Journal of Materials Chemistry A

Accepted Manuscript

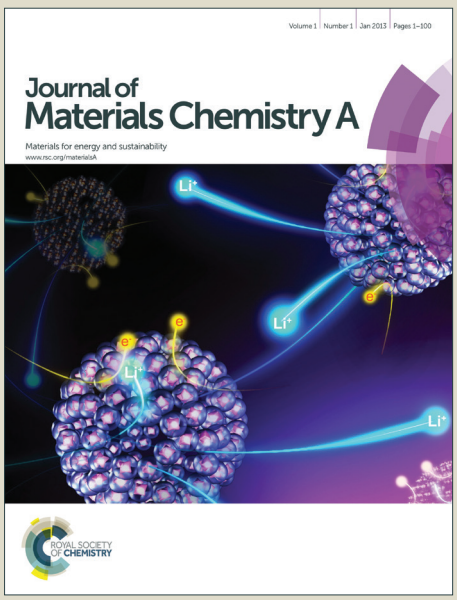

ROYAL SOCIETY OF CHEMISTRY

www.rsc.org/materialsA

MoS_2 Architectures Supported on Graphene Foam/Carbon Nanotube Hybrid Films: Highly Integrated Frameworks with Ideal Contact for Superior Lithium Storage

By Jin Wang, Jilei Liu, Jingshan Luo, Pei Liang, Dongliang Chao, Linfei Lai, Jianyi Lin and Zexiang Shen**

J. Wang, Prof. Z. X. Shen
Energy Research Institute (ERI@N), Interdisciplinary Graduate School, Nanyang Technological University, Research Techno Plaza, 50 Nanyang Drive, 637553, Singapore
E-mail: Zexiang@ntu.edu.sg (Z.X. Shen)
E-mail: Lijy@ntu.edu.sg (J.Y. Lin)

J. Wang, J. L. Liu, J. S. Luo, P. Liang, D. L. Chao, Prof. Z. X. Shen
Division of Physics and Applied Physics, School of Physical and Mathematical Sciences, Nanyang Technological University, 21 Nanyang Link, 637371, Singapore

P. Liang
College of Optical and Electronic Technology, China Jiliang University, Hangzhou 310018, China

L. F. Lai, Prof. J. Y. Lin
Energy Research Institute (ERI@N), Nanyang Technological University, 50 Nanyang Drive, 637553, Singapore

Keywords: molybdenum sulfide, graphene, CNT, flexible, lithium ion batteries

Abstract

Three-dimensional (3D) nanoworm-like MoS_2 architectures have been successfully synthesized and directly supported on graphene foam/carbon nanotubes (GF/CNT) hybrid films. The sp^2-hybridized GF/CNT films provide robust frameworks with ideal contact for the nucleation and subsequent massive growth of MoS_2 architectures, while act as an efficient current collector with conductive contact for binder-free electrodes. The as-prepared hierarchical MoS_2@GF/CNT electrode shows capacities of 1368 mAh g^{-1} and 823 mAh g^{-1} at current densities of 200 mA g^{-1} and 5000 mA g^{-1}, which can retain 81.3% of the initial reversible capacity up to 120 cycles.

Introduction

Ever-growing demand for lithium-ion batteries (LIBs) with ultrafast charging and discharging rates has captivated the attention of many investigators in various applications such as portable electronic devices and electrical vehicles applications.[1-5] In particular, LIBs with high reversible capacity, stable cycle performance, capacitor-like rate performance and high energy density, highly desirable for next generation power sources of electric vehicles, are known to be largely hindered by the lack of suitable electrode materials. Up to now, various electrochemically active materials made of carbonaceous materials[6-10], metal oxides [11-16] and metal sulfides [17-21] have been developed for lithium storage. Especially, layered molybdenum sulfide (MoS_2) has been extensively investigated for anode materials of rechargeable LIBs because it can deliver a higher capacity (~670 mAh g^{-1} with 4-electron transfer reaction per formula) than the commercial graphite material (372 mAh g^{-1}).[22, 23] Unfortunately, a large specific volume change commonly occurs during the cycling processes, resulting in the aggregation of active materials. Thus, the capacity fading and poor rate performance of MoS_2 anode are still the main challenge.

To address these above issues, various strategies have been developed to enhance the electrochemical performance of MoS_2 or MoS_2 composites by using nanotechnologies [24], heterostructures [25-27] and carbon materials[17, 28-40] and carbon materials[17, 28-39] as the conductive matrix. Especially, the sp^2-hybridized carbon nanomaterials (e.g. one-dimensional (1D) carbon nanotubes (CNTs) and two-dimensional (2D) graphene) are the most promising matrix due to superior

mechanical strength, electrical conductivity, and extraordinary adaptability to different interfacial processes.[10, 41, 42] In these systems, decent electrochemical performance has been demonstrated (see a complete list in Table S1 in the Supporting Information). [17, 24, 28-30, 32-38, 43-48] Excellent cycling performance has been achieved by embedding single-layered ultrasmall MoS_2 nanoplates in electrospun carbon nanofibers.[17] Ultrathin MoS_2 nanosheets grown on N-doped graphene sheets have been reported to deliver excellent cyclic stability and high-rate capability.[49] However, in all these works, MoS_2 or MoS_2 composites are in the form of powders and therefore conductive additives and binders are always required.

Recently, an emerging new concept has been exploited to enhance the energy per foot-print area by directly growing electroactive nanostructures on various substrates, especially 3D porous carbon materials as integrated electrodes for LIBs.[11, 13, 14, 30, 42, 45, 50-52] Superior electrochemical performance has been achieved by constructing 3D porous interconnected nanocomposites with 0D MoS_2, 1D CNTs, and 2D graphene on stainless steel or Ni foam. [28] However, the typical loading mass was only around 0.5 mg cm^{-2}. 3D graphene foam (GF) and carbon nanotube (CNT) film have been regarded as excellent backbones for loading MoS_2 nanoparticles due to their lightweight and high conductivity.[30, 42, 45] However, CNTs prefer to form bundles and graphene sheets tend to agglomerate and clump together, leading to their limited external accessible surface area for ions and electrolyte. Graphene foam is usually brittle and can hardly support massive active materials. Compared with their single components, graphene/CNT hybrid films have shown improved physical and

chemical properties, including enhanced electrical conductivity and mechanical flexibility, due to the synergistic effects.[53-57] Moreover, graphene/CNT hybrid films provide increased active surface area for the growth of active materials, leading to the increased areal loading but without aggregation and sacrificing a good electrical contact between the graphene and CNTs.[10, 41] Nonetheless, there is no report on the integrated MoS_2 architectures directly supported on flexible graphene/CNT hybrid films.

In this paper, we present an alternative route to construct few-layer MoS_2 hierarchical architectures on hybrid films consisting of 1D CNTs supported on 3D GF, which is denoted as GF/CNT. The obtained samples, 3D hierarchical MoS_2 architectures supported on GF/CNT substrates are denoted as MoS_2@GF/CNT. This rational design has the following merits: First, GF/CNT acts as both a lightweight scaffold for the growth of 3D MoS_2 architectures and an efficient current collector, which provides fast pathways for electron transportation. Second, the nanoworm-like architectures built from interconnected nanosheets effectively inhibit the aggregation of MoS_2 architectures, while the ion reservoir induced by the void space between sheet-like subunits facilitates the transportation of electrolyte ions, and accommodates the volume change during charge/discharge process. Moreover, the ultrathin nature of MoS_2 nanosheets can effectively reduce the diffusion length of both electrons and ions. Third, the strong adsorption effects between MoS_2 and CNT can provide an energetically favoured process for boosting vast growth of MoS_2 nanosheets onto CNT and immobilizing them, in favour for an increased areal loading but without

aggregation, which can be verified through first-principle ab initio calculations and experimental results. The flexible MoS_2@GF/CNT electrode gives a higher mass loading of ~3 mg cm^{-2}, compared to that of MoS_2@GF electrode prepared with the same condition. Higher areal mass loading of battery electrode materials is preferred which can reduce the number of manufacturing steps for achieving the same total energy and also lower the separator cost. With these merits, our MoS_2@GF/CNT electrode exhibits high reversible capacity, superior high-rate capability and excellent cycling stability.

Experimental

Synthesis of GF/ CNT hybrid films

GF was employed for the subsequent growth of CNTs, which was achieved by chemical vapor deposition (CVD) according to our previous results. [41, 42] For the growth of GF/CNT films, the typical areal mass of GF in this study is about 0.4-0.6 mg cm^{-2}. The NiCo catalyst was deposited on GF through a hydrothermal reaction. Briefly, 0.1 mmol of $Ni(NO_3)_2 \cdot 6H_2O$ and 0.2 mmol of $Co(NO_3)_2 \cdot 6H_2O$ were dissolved in 40 ml of deionized (DI) water to form a clear pink solution. After that, 1.2 mmol of urea was added to the obtained solution. Then, this resulting solution was transferred into Teflon-lined stainless steel autoclave. A piece of GF was fixed on one piece of glass slide by Kapoton tape and immersed into the reaction solution. The autoclave was then sealed and the hydrothermal reaction was conducted at 120 ^oC for 2 h. The GF/NiCo precursor was then annealed in air at 350 ^oC for 1 min and employed directly as the catalyst-loaded substrate for the growth of CNTs at 750 ^oC in

a mixture of C_2H_4, H_2 and Ar with flow rates of 20, 40 and 100 sccm, respectively. H_2 was introduced prior to the growth process in order to activate the catalyst effectively. In order to remove NiCo precursor, the obtained GF/CNT were hydrothermal treated in 35wt% HNO_3 solution at 90 ^oC for 10 h, followed by washing with DI water until neutral pH, and drying at 60°C in an electric oven. A typical areal mass of GF/CNT in this study is about 0.6-0.8 mg cm^{-2}.

Synthesis and Self-assembly of nanoworm-like MoS_2 architectures@GF/CNT

Hierarchical MoS_2 architectures anchored into GF/CNTs were prepared by a P123-assisted solution-phase method. In a typical experiment, the mixed solution was prepared by dissolving 80 mg of thioacetamide (C_2H_5NS, TAA), 40 mg of sodium molybdate and 0.2 g of P123 (a triblock copolymer, $HO(CH_2CH_2O)_{20}(CH_2CH(CH_3)O)_{70}(CH_2CH_2O)_{20}H$) in 30 mL of distilled water. Then, this resulting solution was transferred into Teflon-lined stainless steel autoclave. One piece of GF/CNTs films with an area of 8 cm^2 was fixed on one piece of glass slide by Kapoton tape and immersed into the above solution. The autoclave was then sealed and the hydrothermal reaction was conducted at 200 ^oC for 24 h. After the autoclave was cooled down to room temperature, the samples were rinsed with DI water for several times and then dried at 60°C in an electric oven. The achieved samples were thermally decomposed in a tube furnace at 400 ^oC for 2 h under H_2/Ar (5:95 v/v) atmosphere with a heating rate of 10 ^oC min^{-1}. The weight of MoS_2 in the 3D architectures is calculated by weighting the obtained sample before and after reaction. The obtained nanoworm-like MoS_2 architectures anchored into GF/CNTs is denoted

as MoS_2@GF/CNT. For the comparison, MoS_2 grown on GF was prepared by the same process and denoted as MoS_2@GF. Before the hydrothermal reaction, the GF/CNT film treated by oxygen plasma with a constant oxygen flow maintained at 80 sccm for 100 seconds.

Cell Assembly and Electrochemical Measurements

To test the anode performance of all synthesised materials, CR 2016 coin cells were made using Celgard 2400 as the separator and 1M $LiPF_6$ in ethylene carbonate-diethylene carbonate (EC:DEC=1:1) as the electrolyte. Li-metal was used as the counter and reference electrode. The coin cells were assembled inside an argon-filled glovebox with oxygen and water contents below 1 and 0.1 ppm, respectively. The obtained MoS_2@GF/CNTs and MoS_2@GF were punched to a disk-shaped electrode with a diameter of 12 mm for the electrochemical measurements, which were directly used as working electrodes and assembly into coil cells without adding any conductive or binding materials. Galvanostatic charging and discharging tests were conducted using a battery tester (NEWARE) at different current rates. It should be noted that all the specific capacities reported in this work are based on the total mass of the composites rather than the mass of MoS_2 only. Cyclic voltammetry (CV) was performed using an electrochemical workstation (CHI 760D, Chenhua, Shanghai) from 10 mV to 3 V at a scanning rate of 0.5 mV s^{-1}. Electrochemical impedance spectroscopy (EIS) were also carried out with an electrochemical workstation over a frequency range from 10^6 Hz to 100 mHz at open circuit potential after two galvanostatic charging and discharging cycles at 100 mA g^{-}

[1].

Characterization

The morphology and structure characterization of the samples were carried out by transmission electron microscope (TEM, JOEL JEM 2100F), scanning electron microscopy (FESEM, Model JSM-7600F, JEOL Ltd., Tokyo, Japan), and X-ray diffraction (XRD, Bruke D8). Raman spectroscopy was recorded by Renishaw Raman Microscopy with 2.33 eV (532 nm) excitation laser. The XPS measurements were performed with a VG ESCALAB 220i-XL system using a monochromatic Al Kα1 source (1486.6 eV). All XPS spectra were obtained in the constant pass energy (CPA) mode. The pass energy of analyser was set to be 10 eV to have high measurement accuracy. The binding energy scale was calibrated with pure Au, Ag and Cu by setting the Au $4f_{7/2}$, Ag $3d_{5/2}$, and Cu $2p_{3/2}$ at binding energy of 84.0, 368.3, and 932.7 eV, respectively. The surface area analysis was conducted using Brunauer–Emmett–Teller surface area analyzer (BET, Micromeritics ASAP2020).

First-principle theoretical calculations

Theoretical calculations were carried out using first-principle density functional theory (DFT) based calculations using the Vienna Ab-Initio Simulation Package (VASP). In our calculations, projector-augmented-wave (PAW) potentials were used to account for the electron-ion interactions, while electron exchange–correlation (xc) interactions were treated using a generalized gradient approximation (GGA) in the Perdew–Burke–Ernzerhof (PBE) version. The stabilities of the mixed system were manually modelled by absorption of MoS_2 clusters onto graphene and CNT. The

optimization of the plane wave codes, volume and cell generally affects the calculations of Pulay stress, leading to incorrect calculations of the diagonal components of the stress tensor. Therefore, we need high cut-off energy for the plane wave basis sets to obtain a reliable stress tensor. Here, 480 eV of cut-off energy was taken for our calculations.

Results and Discussions

The fabrication process of the MoS_2@GF/CNT electrode is depicted in **Figure 1**. The catalyst-assisted CVD-derived GF/CNT is directly employed as 3D light-weight frameworks for the growth of hierarchical MoS_2 architectures, which are achieved by a hydrothermal reaction between sodium molybdate and TAA with the help of the surfactant P123. The 3D MoS_2 architectures are anchored into the skeleton of GF/CNT films by spontaneous self-assembly of MoS_2 nanosheets. The mass of MoS_2 in the 3D architectures is calculated by weighting the obtained sample before and after reaction. It should be noted that the as-prepared MoS_2@GF/CNT was directly employed as the electrode of half-cells for tests without conducting carbon, polymer binder and current collector. Figures S1-2 show the morphology and microstructure of GF and GF/CNT. The weight fractions of MoS_2 in the obtained electrodes can be rationally controlled by adjusting the concentration of the reactants (sodium molybdate and TAA) using the GF/CNT films with nearly the same area (**Figure S3**). We also fabricated MoS_2 sheets on other conductive substrates, including graphene foam, carbon cloths, stainless steel and titanium foil (Figures S4-6), which proves the versatility of our synthesis method.

The morphology and phase of the as-prepared MoS_2@GF/CNT were systematically investigated by field-emission scanning electron microscopy (FE-SEM) and X-ray diffraction (XRD). **Figure S7** shows the photograph and good flexibility of MoS_2@GF/CNT electrode with a size of 2 cm×4 cm. The obtained sample can be bent or fold without any protective case and will neither break, nor will the nanosheet layer peel off during repeated bending or folding. Hence, MoS_2@GF/CNT can be directly employed as a freestanding electrode without the need of conventional binders, conductive additives and metallic current collectors. **Figures 2a and b** show the 3D network morphology with branches of 60−100 μm and macropores of 150−500 μm. Further well-defined interconnected network structure is shown in **Figure 2c**, where the graphene foam is uniformly covered with a layer of MoS_2@CNT nanoworm-like architectures. In addition, the corresponding cross-sectional images reveal that MoS_2@CNT architectures are grown on the outer and inner surfaces of GF backbones as shown in **Figures 2d-e** (see the corresponding elemental mapping images in Figure S8). From SEM images at high magnification (**Figure 2f**), we can clearly see the highly interconnected and porous 3D nanoworm-like architectures built from numerous ultra-thin MoS_2 nanosheets branching uniformly on CNT surface. Further investigations show that the building block nanosheets with lateral sizes of ~100 nm are randomly continuous and interconnected with each other, forming a highly porous nanonanoworm-like morphology (**Figure 2g**). We consider that this internal cross-linked structure would effectively restrain both lamellar aggregation and mechanical failure (leading to the

disconnection of active materials from the current collector) after repeated charge/discharge processes, and hence can efficiently maintain the long-standing existence of nanosheets and good electrical contact. Besides, the interconnected nanosheets form a large amount of voids between each other, with sizes from 50 nm to several hundred nm, which are possibly derived from the self-assembly process. These internal voids between sheet-like subunits serve as an "ion reservoir" to allow for an easy diffusion of electrolyte ions, while accommodating the volume change during lithium insertion and extraction.

During the reaction, the growth of MoS_2 sheets is found to be favourably selective on GF/CNT, with little free particle growth in solution. Obviously, GF/CNT provides a novel substrate for the nucleation and subsequent growth of MoS_2 crystals. The selective growth of MoS_2 on GF was attributed to the interactions between functional groups of GF/CNT and MoO_4^{2-} precursors with the help of surfactant P123. The amphiphilic P123 triblock copolymer can bond with the functional groups of GF/CNT, which was created after plasma treatment. The possible reaction on the surface of GF/CNT may be expressed as follows:

$$CH_3CSNH_2 + H_2O \rightarrow CH_3CONH_2 + H_2S \quad (1)$$

$$MoO_4^{2-} + 3H_2S \rightarrow MoS_2 + 3H_2 + SO_4^{2-} \quad (2)$$

The XRD patterns of the bare GF/CNT and MoS_2@GF/CNT composites are displayed in **Figure 2h**. The as-grown GF/CNT substrates show a typical diffraction peaks at 26.5 ^{o}, corresponding to the (002) reflection of graphitic carbon, respectively (JCPDS card no. 75-1621). The highly crystalline structure of GF/CNT is very

favourable for the electron transfer and ion diffusion. By comparison, the detected peaks at 2θ=14.1, 32.3, 39.4 and 58.7 ° in the pattern of MoS_2@GF/CNT composites can be assigned to the (002), (100), (103) and (110) planes in the hexagonal phase MoS_2 (a=b=0.316 nm, c=1.230 nm, JCPDS card no. 37-1492). Raman spectroscopy was employed to further investigate the structures of the bare GF/CNT and MoS_2@GF/CNT composites (**Figure 2i**). The two characteristic peaks at 1580 and 2720 cm^{-1} correspond to the G and 2D bands, respectively. The 2D/G intensity ratio as well as the absence of the D peak at 1350 cm^{-1} in the spectrum of GF suggests the high quality of GF/CNT before MoS_2 growth. In comparison, the appearance of the D band at 1350 cm^{-1} after MoS_2 growth is an indication of presence of sp^3 bonding which in turn shows a strong coupling between the MoS_2 and the GF/CNT scaffold. The MoS_2@GF/CNT composites have two obvious peaks at 383 cm^{-1} and 405 cm^{-1}, which correspond to E^1_{2g} and A^1_g Raman modes of MoS_2, respectively.

The detailed microstructure of MoS_2@GF/CNT electrodes was further studied by TEM and high-resolution TEM (HRTEM). The MoS_2@GF/CNT composites were sonicated in ethanol for 30 min, which were then dropped onto a TEM grid and dried at ambient conditions. **Figures 3a** and b show the typical TEM images of MoS_2 branch anchored into CNTs. Most of the building blocks in hierarchical nanostructures are 3~5 layers of MoS_2 as displayed in **Figure 3c**. Typical lamellar structure with different interlayer spacing of 0.67 and 0.69 nm can be observed from the HRTEM image (**Figure 3d**). The inset fast Fourier transformation (FFT) pattern in the inner square area reveals the orientation of layers along the [002] direction of

CNTs (**Figure 3d**). Interplanar spacing of 0.35 nm can also be observed, which is in good consistence with the d spacing of (002) planes of CNTs. To further reveal the elemental distribution in individual single hybrid nanotube of MoS_2@GF/CNT, scanning TEM-based energy dispersive spectroscopy (STEM-based EDS) was used to obtain line scans and mapping analysis, shown in **Figures 3e-i**, unambiguously demonstrating CNT-core/MoS_2-branch hierarchical structure. EDS spectrum is consistent with the mapping result shown in **Figure 3j**.

X-ray photoelectron spectroscopy (XPS) was used to investigate the chemical states of Mo and S in MoS_2@GF/CNT composites as shown in **Figures 4a** and **b**. The peaks of Mo $3d_{3/2}$ and Mo $3d_{5/2}$ are located at binding energies of 232.5 and 229.3 eV, respectively, which are the characteristic peaks of Mo^{4+} in MoS_2. The S 2p peaks at 162 and 163.2 eV are attributed to S^{2-} of MoS_2. [28] Full nitrogen adsorption/desorption isotherms of MoS_2@GF/CNT composites were measured to obtain the information of the pore size distribution and specific surface area. As shown in **Figure 4c**, a type-IV isotherm with a type-H3 hysteresis loop in the relative pressure range of 0.45-1.0 P/P_0 indicates the presence of mesoporous structure. Accordingly, the specific surface area is calculated to be 168 $m^2\ g^{-1}$ via the Brunauer-Emmett-Teller (BET) method. The pore size distribution derived from the BJH method is given in the inset of **Figure 4d**. The sharp peak at 34.1 nm is attributed to mesoporous channels in MoS_2@GF/CNT architectures. Besides, the sharp peak at 124.8 nm corresponds to macropores. Such a high specific surface area of MoS_2@GF/CNT composites with massive mesopores and macropores could be

desirable for energy storage application or other applications. These mesopores and macropores in the 3D MoS_2@GF/CNT architectures can serve as an "ion and electrolyte reservoir" to facilitate the transportation of electrolyte ions, and can also buffer the volume change to prevent mechanical failure for superior stability and cyclability.

In strong contrast, highly interconnected blanket-like architectures built from numerous MoS_2 nanosheets are uniformly distributed on GF, in the absence of CNTs (**Figure 5a** and **b**). The inset of **Figure 5a** reveals the 3D network morphology of MoS_2@GF with branches of 60−100 μm. Further investigations show that the building nanosheets have lateral sizes of ~100 nm, and they are randomly connected with the adjacent nanosheets to self-assemble into continuous and porous blanket-like architectures on GF, which shows a specific surface area of 28.9 m^2 g^{-1} as in Figure S9. A typical TEM image in **Figure 5c** shows the intrinsic wrinkles or corrugations of MoS_2 nanosheets distributed on GF. The selected area electron diffraction (SAED) pattern in the inset of **Figure 5c**, clearly demonstrates a polycrystalline structure of MoS_2. Typical lamellar structure with interlayer spacing of 0.66 nm can be observed from the HRTEM image (**Figure 5d**). The typical layer number of MoS_2 sheets is 3-5. The typical mass loading of MoS_2 nanosheets on GF prepared with the same synthesis process is only ~0.5-0.8 mg cm^{-2}. In contrast, the typical mass loading of nanoworm-like MoS_2 architectures grown on GF/CNT is estimated to be ~3 mg cm^{-2}. The obvious morphological difference and areal loading of active materials highlight the important role of GF/CNT films as a novel framework in mediating the growth of

nanomaterials.

The electrochemical properties of MoS_2@GF/CNT were further evaluated. MoS_2@GF/CNT was directly used as the electrode of half-cells for tests without conducting carbon, polymer binder and current collector. As a control experiment for comparison, MoS_2@GF electrode was also employed as the testing electrode. The CV curves of MoS_2@GF/CNT during the first 4 cycles are presented in **Figure 6**a. During the first cycle, there are two reduction peaks located at 0.4 and 0.9 V and two oxidation peaks located at 1.8 and 2.3 V. The reduction peak at 0.9 V can be attributed to Li insertion into the interlayers of MoS_2, accompanied by phase transformation from 2H to 1T structures of Li_xMoS_2. The second obvious reduction peak at 0.4 V corresponds to the reduction of Li_xMoS_2 to Mo metal and Li_2S, which is based on the following conversion reaction: [23, 24]

$$MoS_2 + 4Li^+ + 4e^- \rightarrow Mo + 2Li_2S \qquad (3)$$

The oxidation peak at 1.8 V can be ascribed to partial oxidation of Mo to form MoS_2 due to the defect sites. The following distinct peak located at 2.3 V is associated with the oxidation of Li_2S to S. After the first cycle, the electrode is mainly composed of Mo and S instead of the initial MoS_2. [36] The dominant reduction peak at 1.8 V is well known in lithium-sulfur battery and is attributed to the formation of Li_2S, and the smaller peak at 1.1 V can be the conversion of residual S_8^{2-} to Li_2S. [36, 58] Accordingly, the oxidation peak at 2.3 V is related to the oxidation of Li_2S to S. The shape of CV curve and the oxidation/reduction peaks can still retain, indicating the good stability of the electrochemical process after several cycles.

Figure 6b displays the representative charge/discharge profiles of MoS_2@GF/CNT at a current density of 100 mA g^{-1}. In agreement with the CV curves, two potential plateaus at around 1.1–1.4 V and 0.6 V can be observed during the first discharge (lithiation) process. The former was attributed to the Li insertion reaction that led to the formation of Li_xMoS_2, whereas the latter at 0.6 V was related to a conversion reaction of MoS_2 to Mo particles. The MoS_2@GF/CNT electrode delivers initial discharge and charge capacities of 1568 and 1252 mAh g^{-1}, respectively, giving a Coulombic efficiency of 79.8%. However, the bare GF/CNT electrode can only deliver initial discharge and charge capacities of 592 and 294 mAh g^{-1}, respectively (**Figure S12**), which is almost the similar level as that of GF electrode(see **Figure S11**). Such high initial lithium storage may be attributed to the unique 3D graphene-backboned nanoworm-like MoS_2@CNT architectures. The irreversible capacity loss of around 300 mAh g^{-1} is mainly due to the irreversible process such as the formation of the SEI layer, the electrolyte decomposition and reduction of oxygen-containing groups. The Coulombic efficiency rapidly reaches more than 99% after the second cycle. The second and third discharge profiles are almost coinciding with each other, exhibiting excellent cycling performance. The potential plateaus at 1.8 V and 1.1 V (Figure 6b) are also in agreement with the two peaks of the CV curves in Figure 6a. The cycling performance is also outstanding: even after 120 cycles, both the discharge and charge capacities of the MoS_2@GF/CNT electrode are stable at about 1112 mAh g^{-1} at the current density of 200 mA g^{-1}, delivering nearly 81.3% capacity retention (Figure 6c). In contrast, the MoS_2@GF electrode shows

continuous and progressive capacity decay under the same testing conditions. After 120 cycles, MoS_2@GF electrode only delivers a capacity of 766 mAh g^{-1}. The excellent rate retention of MoS_2@GF/CNT is shown in Figure 6d. The specific capacities of 1064 and 1006 mAh g^{-1} can be maintained at high rates of 1 and 2 A g^{-1}, respectively. Even cycled at a high current of 5 A g^{-1}, the specific capacities of 823 mAh g^{-1} can be maintained. Remarkably, these values are much higher than that of MoS_2@GF (565 mAh g^{-1}). Moreover, after deep cycling at 5 A g^{-1}, the specific capacity is recovered to the same levels as previous measurement when the current is returned back to 100 mA g^{-1}. Even after 120 cycles at a high current density of 1 A g^{-1}, the discharge capacity can be stabilized at 936.3 mAh g^{-1} as shown in Figure S10. A complete comparison of electrochemical properties of these two samples, summarized in **Table S2**, shows that MoS_2@GF/CNT possesses excellent electrochemical properties, including high initial Coulombic efficiency, high specific capacity, high rate performance and stable cyclability. Indeed, the TEM image of the MoS_2@GF/CNT electrode after cycling shows that the clusters of active material are still anchored on CNT (shown in Figure S13).

To gain better insight into the reason of the unique 3D graphene-backboned nanoworm-like MoS_2@CNT architectures for boosting lithium storage, we performed electrochemical impedance spectroscopy (EIS) for both electrodes as shown in **Figure 6e.** Obviously, the diameter of the semicircle for the MoS_2@GF/CNT in the high-medium frequency region is smaller than that of MoS_2@GF, which indicates that MoS_2@GF/CNT possesses the lower contact and charge-transfer resistances. The

kinetic differences of both MoS_2 electrodes were further investigated using the R–C equivalent circuit. The high and medium frequency semicircle in Figure 6e could be attributed to the resistance R_{sf} and CPE1 of the SEI film, the medium frequency semicircle to the charge transfer resistance of the electrode reaction R_{ct} and CPE2 of the electrode-electrolyte interface, and the inclined line in the low frequency region to lithium-ion diffusion processes. R_{sf} and R_{ct} can be obtained by fitting data according to the equivalent circuit model in Figure 6e. R_{sf} and R_{ct} of MoS_2@GF/CNT electrode are 4.32 and 12.35 Ω, respectively, which are much lower than those of MoS_2@GF (R_{sf}=8.75 and R_{ct}=28.64 Ω). For both samples, the solution resistances are almost the same due to the same electrolyte testing system. In contrast, the charge transfer resistance of MoS_2@GF/CNT is much lower than that of MoS_2@GF, clearly demonstrating a better electrochemical activity of MoS_2@GF/CNT for lithium-ion storage. This result clearly validates that nanoworm-like MoS_2 architectures based on GF/CNT hybrid films not only ensure a high electrical conductivity of the overall electrode, but also remarkably enhance the electrochemical activity of MoS_2 anode during the cycle processes.

Therefore, it is not difficult to understand the reason for the enhanced lithium ion storage and improved high rate performance of MoS_2@GF/CNT, which has the several well-known characteristics: (a) The unique nanoworm-like MoS_2 architectures are homogenously anchored into the skeleton of GF/CNT with a close and robust physical contact, which provides fast electronic conduction channels and ensures the individual MoS_2 nanosheets electrically connected during charge/discharge cycles. (b)

The large internal void between sheet-like subunits serves as an "ion reservoir" to allow for an easy diffusion of electrolyte ions and high contact between MoS_2 nanosheets and electrolyte, while also accommodating the volume change during lithium insertion and extraction. Hence, this 3D interpenetrating structure not only provides an excellent ion transport from the electrolyte to active materials on GF/CNT, but also from active materials to the current collector, as shown in Figure 6e.

In addition to the above two significant merits for boosting LIB performance, the most striking feature of our MoS_2@GF/CNT architectures is that GF/CNTs films provide an ideal interface for boosting vast MoS_2 growth (with a loading of 3 mg cm^{-2}) and fast electronic conduction transportation for active materials (lower resistance). In order to better understand the interesting CNT and graphene interfaces on immobilizing MoS_2, we performed first-principle density functional theory (DFT) using Vienna Ab-initio Simulation Package (VASP) to explore the adsorption energy of MoS_2 on the surface of graphene and CNT. For the molecule-surface interaction, we calculate the adsorption energy based on the equation:

$E_{ab}=(E_{total}-E_G-E_{MoS_2-C})/n$, where E_{total}, E_G and E_{MoS_2-C} denote the total energies of the calculated system, graphene nanosheet (CNT) and MoS_2, respectively, and n is the number of MoS_2 units. For the calculation, the same numbers of MoS_2 and C atoms are used in the calculated models, where contains 20 MoS_2 units and 216 carbon atoms. The cross-section illustration of MoS_2 bonding with graphene and CNT is shown in **Figure S14**. Here, we calculated adsorption energies of MoS_2 on the surfaces of CNTs with the various chiral indices ((10, 10), (12, 12), (15, 15), (18, 18)

and (25, 25)). The calculated adsorption energies of MoS_2 at various active sites of graphene and CNT with different diameters are listed in **Table S3**. The results indicate the CNTs have stronger adsorption energy with MoS_2 compared to graphene. Based on the fitted function relationship between the adsorption energies and diameters of CNT (**Figure S15**), it is found that the CNTs with smaller diameters have stronger adsorption energy with MoS_2. In our study, the typical diameters of CNTs vary between 20 and 80nm, and the calculated adsorption energies of MoS_2 on CNTs are nearly close to -18.98 meV, which is stronger than that on graphene (−18.7 meV). Obviously, it is found that MoS_2 preferentially adsorbs on CNT rather than graphene, demonstrating an evident synergistic effect in the MoS_2@GF/CNT electrode. Actually, the experimental results (the higher areal loading of MoS_2 on GF/CNT) can also support our calculation results. The Raman result of the appearance of the D band at 1350 cm^{-1} after MoS_2 growth on GF/CNT verifies the presence of sp^3 bonding indicating a strong coupling between the MoS_2 and the GF/CNT scaffold. Also, we compare the Raman spectra of E_{2g}^1 and A_{1g} modes of MoS_2@GF/CNT (**Figure S16**). Blue shifting of 3~5 cm^{-1} for A_{1g} and E_{2g}^1 modes can be observed in the sample of MoS_2@GF/CNT, which also verifies the strong coupling between MoS_2 and CNT (or GF), resulting in the structure changes of MoS_2 nanosheets. Blue shifting is mainly due to the change of the force constant resulted from the change of the interlayer Van der Waals force in MoS_2 layers (for A_{1g} mode) and the structure changes or long-range Coulombic interlayer interactions (for E_{2g}^1 mode).[59] Herein, GF/CNTs provide an ideal interface with the strong adsorption effects for vast growth of MoS_2

nanosheets without aggregation, which effectively enhance the stability of active materials. Therefore, a close and robust conductive contact between MoS_2 and CNTs, and the strong coupling between graphene and CNTs render the intact wire-up framework during the repeated charge and discharge processes, resulting in the maximization of synergistic interaction.

Conclusions

In summary, we have designed and successfully fabricated nanoworm-like MoS_2 architectures@GF/CNT as self-supported, binder-free anode electrodes. The rational sp^2-hybridized 3DGF/CNT provides a novel substrate for the nucleation and massive growth of nanoworm-like MoS_2 architectures, which are well-defined by self-assembly of ultrathin nanosheets. Also, the highly integrated frameworks can provide an ideal conductive contact between MoS_2 and CNT, resulting in the maximization of synergistic interaction. Such unique MoS_2@GF/CNT architectures with robust interface synergistic effect makes it as a new class of anode materials for developing LIBs with very high energy and power densities as well as extremely high cyclability. High discharge capacities of 1368 mAh g^{-1} and 823 mA h g^{-1} at current densities of 200 mA g^{-1} and 5 A g^{-1} are achieved, which can retain 81.3% of the initial reversible capacity after 120 cycles. These results clearly demonstrate the strong synergistic effect of MoS_2@GF/CNT. Density Functional theory (DFT) calculations reveal the existence of the strong absorption energy between MoS_2 and CNT, which can provide energetically favoured processes for boosting vast growth of MoS_2 nanosheets onto CNT and maintaining the electrode integration during the repeated

charge and discharge processes. The technique demonstrated here can be easily used with other batteries chemistry with higher energy density and power density. This work also offers a facile and ingenious design concept to combine the sp^2-hybridized GF/CNT films with nanostructured materials, which can be readily generalized to other materials, to build multifunctional flexible electrodes for a large spectrum of device applications.

References

1 J. M. Tarascon and M. Armand, *Nature*, 2001, **414**, 359-367.

2 V. Etacheri, R. Marom, R. Elazari, G. Salitra and D. Aurbach, *Energy Environ. Sci.*, 2011, **4**, 3243-3262.

3 N. S. Choi, Z. Chen, S. A. Freunberger, X. Ji, Y. K. Sun, K. Amine, G. Yushin, L. F. Nazar, J. Cho and P. G. Bruce, *Angew. Chem. Int. Ed.*, 2012, **51**, 9994-10024.

4 J. B. Goodenough and K.-S. Park, *J. Am. Chem. Soc.*, 2013, **135**, 1167-1176.

5 H. Li, Z. Wang, L. Chen and X. Huang, *Adv. Mater.*, 2009, **21**, 4593-4607.

6 X. Huang, X. Qi, F. Boey and H. Zhang, *Chem. Soc. Rev.*, 2012, **41**, 666-686.

7 M. Pumera, *Energy Environ. Sci.*, 2011, **4**, 668-674.

8 Z. A. Qiao, Q. Huo, M. Chi, G. M. Veith, A. J. Binder and S. Dai, *Adv. Mater.*, 2012, **24**, 6017-6021.

9 L. Liu, Z. Niu, L. Zhang, W. Zhou, X. Chen and S. Xie, *Adv. Mater.*, 2014, **26**, 4855-4862.

10 J. Liu, L. Zhang, H. B. Wu, J. Lin, Z. Shen and X. W. Lou, *Energy Environ. Sci.*, 2014.

11 S. Liu, Z. Wang, C. Yu, H. B. Wu, G. Wang, Q. Dong, J. Qiu, A. Eychmüller and X. W. Lou, *Advanced Materials*, 2013, **25**, 3462-3467.

12 J. Wang, L. Li, C. L. Wong, L. Sun, Z. Shen and S. Madhavi, *RSC Adv.*, 2013, **3**, 15316.

13 J. Wang, L. Li, C. L. Wong and S. Madhavi, *Nanotechnology*, 2012, **23**, 495401.

14 D. Chao, X. Xia, J. Liu, Z. Fan, C. F. Ng, J. Lin, H. Zhang, Z. X. Shen and H. J. Fan, *Adv. Mater.*, 2014, **26**, 5794-5800.

15 Y. Tang, Y. Zhang, J. Deng, J. Wei, H. Le Tam, B. K. Chandran, Z. Dong, Z. Chen and X. Chen, *Adv. Mater.*, 2014, **26**, 6111-6118.

16 J. Wang, N. Yang, H. Tang, Z. Dong, Q. Jin, M. Yang, D. Kisailus, H. Zhao, Z. Tang and D. Wang, *Angew. Chem. Int. Ed.*, 2013, **52**, 6417-6420.

17 C. Zhu, X. Mu, P. A. van Aken, Y. Yu and J. Maier, *Angew. Chem. Int. Ed.*, 2014, **53**, 2152-2156.

18 J. Xie, S. Liu, G. Cao, T. Zhu and X. Zhao, *Nano Energy*, 2013, **2**, 49-56.

19 J.W. Seo, J.T. Jang, S.W. Park, C. Kim, B. Park and J. Cheon, *Adv. Mater.*, 2008, **20**, 4269-4273.

20 B. Luo, Y. Fang, B. Wang, J. Zhou, H. Song and L. Zhi, *Energy Environ. Sci.*, 2012, **5**, 5226-5230.
21 P. P. Wang, H. Sun, Y. Ji, W. Li and X. Wang, *Adv. Mater.*, 2014, **26**, 964-969.
22 E. Benavente, M. A. Santa Ana, F. Mendizábal and G. González, *Coord. Chem. Rev.*, 2002, **224**, 87-109.
23 T. Stephenson, Z. Li, B. Olsen and D. Mitlin, *Energy Environ. Sci.*, 2014, **7**, 209-231.
24 H. Liu, D. Su, R. Zhou, B. Sun, G. Wang and S. Z. Qiao, *Adv. Energy Mater.*, 2012, **2**, 970-975.
25 L. Pan, X. D. Zhu, X. M. Xie and Y. T. Liu, *J. Mater. Chem. A*, 2015, **3**, 2726-2733.
26 X. D. Zhu, K. X. Wang, D. J. Yan, S. Le, R. J. Ma, K. Sun and Y. T. Liu, *Chem. Commun.*, 2015.
27 L. Pan, Y. T. Liu, X. M. Xie and X. D. Zhu, *Chem.–Asian J.*, 2014, **9**, 1519-1524.
28 C. B. Zhu, X. K. Mu, P. A. van Aken, J. Maier and Y. Yu, *Adv. Energy Mater.*, 2015, **5**, DOI:10.1002/aenm.201401170.
29 Z. Wan, J. Shao, J. Yun, H. Zheng, T. Gao, M. Shen, Q. Qu and H. Zheng, *Small*, 2014, **10**, 4975-4981.
30 C. Lu, W. W. Liu, H. Li and B. K. Tay, *Chem. Commun.*, 2014, **50**, 3338-3340.
31 D. J. Li, U. N. Maiti, J. Lim, D. S. Choi, W. J. Lee, Y. Oh, G. Y. Lee and S. O. Kim, *Nano Lett.*, 2014, **14**, 1228-1233.
32 D. B. Kong, H. Y. He, Q. Song, B. Wang, W. Lv, Q. H. Yang and L. J. Zhi, *Energy Environ. Sci.*, 2014, **7**, 3320-3325.
33 L. Yang, S. Wang, J. Mao, J. Deng, Q. Gao, Y. Tang and O. G. Schmidt, *Adv. Mater.*, 2013, **25**, 1180-1184.
34 Y. Shi, Y. Wang, J. I. Wong, A. Y. Tan, C. L. Hsu, L. J. Li, Y. C. Lu and H. Y. Yang, *Sci. Rep.*, 2013, **3**, 2169.
35 G. Huang, T. Chen, W. Chen, Z. Wang, K. Chang, L. Ma, F. Huang, D. Chen and J. Y. Lee, *Small*, 2013, **9**, 3693-3703.
36 J. Xiao, X. J. Wang, X. Q. Yang, S. D. Xun, G. Liu, P. K. Koech, J. Liu and J. P. Lemmon, *Adv. Funct. Mater.*, 2011, **21**, 2840-2846.
37 H. Hwang, H. Kim and J. Cho, *Nano Lett.*, 2011, **11**, 4826-4830.
38 K. Chang and W. Chen, *ACS Nano*, 2011, **5**, 4720-4728.
39 H. Jiang, D. Ren, H. Wang, Y. Hu, S. Guo, H. Yuan, P. Hu, L. Zhang and C. Li, *Adv. Mater.*, 2015, DOI: 10.1002/adma.201501059.
40 Z. Q. Duan, Y. C. Sun, Y. T. Liu, X. M. Xie and X. D. Zhu, *RSC Adv.*, 2014, **4**, 41543-41550.
41 J. Liu, M. Chen, L. Zhang, J. Jiang, J. Yan, Y. Huang, J. Lin, H. J. Fan and Z. X. Shen, *Nano Lett.*, 2014, **14**, 7180-7187.
42 J. Wang, J. Liu, D. Chao, J. Yan, J. Lin and Z. X. Shen, *Adv. Mater.*, 2014, **26**, 7162-7169.
43 J. Xiao, D. Choi, L. Cosimbescu, P. Koech, J. Liu and J. P. Lemmon, *Chem. Mater.*, 2010, **22**, 4522-4524.
44 K. Chang and W. Chen, *Chem. Commun.*, 2011, **47**, 4252-4254.
45 X. Cao, Y. Shi, W. Shi, X. Rui, Q. Yan, J. Kong and H. Zhang, *Small*, 2013, **9**, 3433-3438.
46 Y. Gong, S. Yang, Z. Liu, L. Ma, R. Vajtai and P. M. Ajayan, *Adv. Mater.*, 2013, **25**, 3979-3984.

47 J. Z. Wang, L. Lu, M. Lotya, J. N. Coleman, S. L. Chou, H. K. Liu, A. I. Minett and J. Chen, *Adv. Energy Mater.*, 2013, **3**, 798-805.
48 Y. Chen, B. Song, X. Tang, L. Lu and J. Xue, *Small*, 2014, **10**, 1536-1543.
49 K. Chang, D. Geng, X. Li, J. Yang, Y. Tang, M. Cai, R. Li and X. Sun, *Adv. Energy Mater.*, 2013, **3**, 839-844.
50 J. Luo, J. Liu, Z. Zeng, C. F. Ng, L. Ma, H. Zhang, J. Lin, Z. Shen and H. J. Fan, *Nano Lett.*, 2013, **13**, 6136-6143.
51 H. Yu, C. Zhu, K. Zhang, Y. Chen, C. Li, P. Gao, P. Yang and Q. Ouyang, *J. Mater. Chem. A*, 2014, **2**, 4551-4557.
52 Y. T. Liu, X. D. Zhu, Z. Q. Duan and X. M. Xie, *Chem. Commun.*, 2013, **49**, 10305-10307.
53 H. J. Peng, J. Q. Huang, M. Q. Zhao, Q. Zhang, X. B. Cheng, X. Y. Liu, W. Z. Qian and F. Wei, *Adv. Funct. Mater.*, 2014, **24**, 2772-2781.
54 B. Luo, S. Liu and L. Zhi, *Small*, 2012, **8**, 630-646.
55 Y. Huang, J. Liang and Y. Chen, *Small*, 2012, **8**, 1805-1834.
56 H. Wang and H. Dai, *Chem. Soc. Rev.*, 2013, **42**, 3088-3113.
57 S. Han, D. Wu, S. Li, F. Zhang and X. Feng, *Small*, 2013, **9**, 1173-1187.
58 X. Fang, X. Guo, Y. Mao, C. Hua, L. Shen, Y. Hu, Z. Wang, F. Wu and L. Chen, *Chem.–Asian J.*, 2012, **7**, 1013-1017.
59 H. Li, Q. Zhang, C. C. R. Yap, B. K. Tay, T. H. T. Edwin, A. Olivier and D. Baillargeat, *Adv. Funct. Mater.*, 2012, **22**, 1385-1390.

Figures and Tables

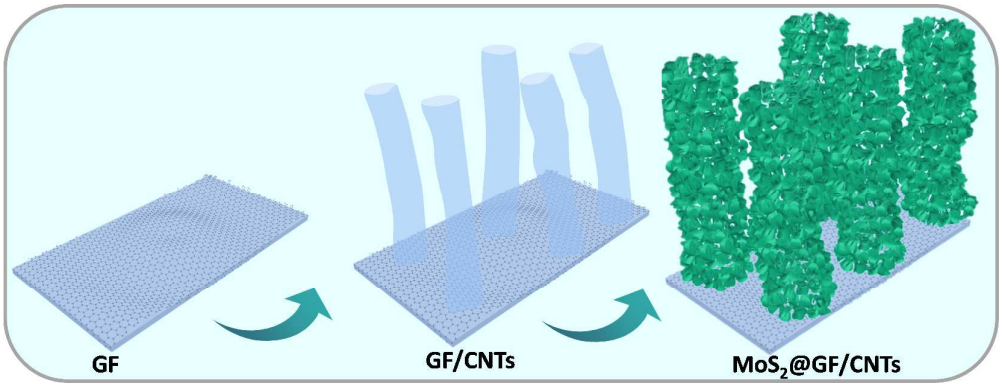

Figure 1 Schematics of the fabrication of MoS_2@GF/CNT electrode.

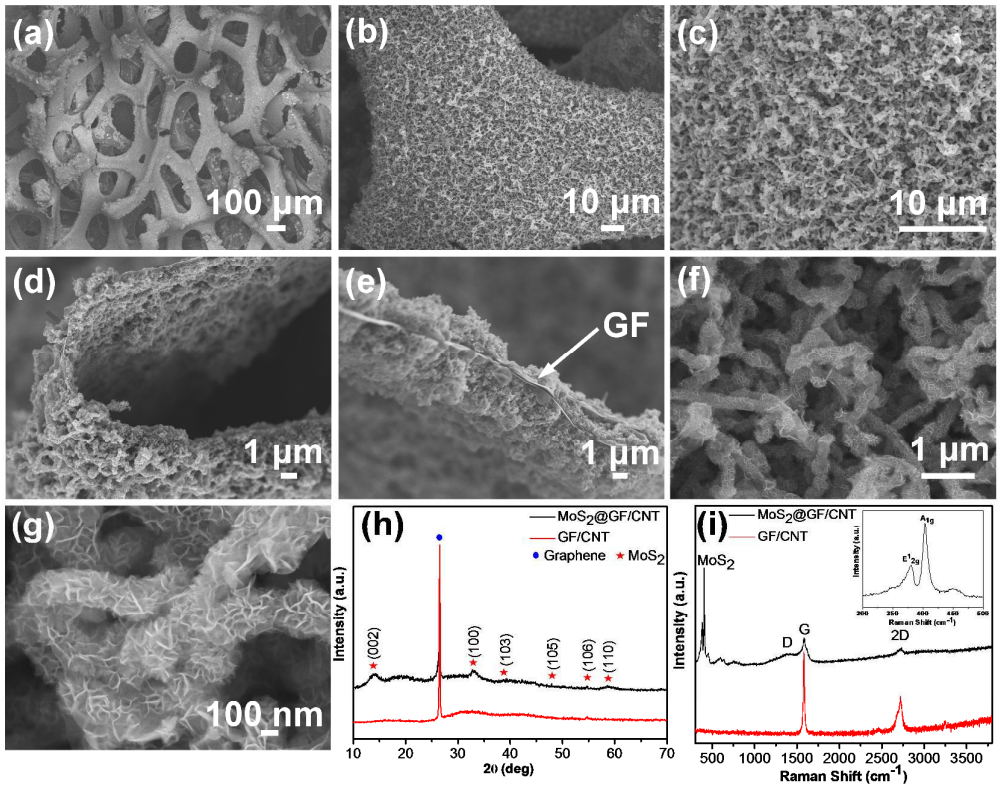

Figure 2 (a-c) Top-view SEM images. (d-e) Cross-sectional images. (f-g) SEM images at high magnification of MoS_2@GF/CNT. (h) and (i) XRD pattern and Raman spectra of MoS_2@GF/CNT and GF/CNT composites.

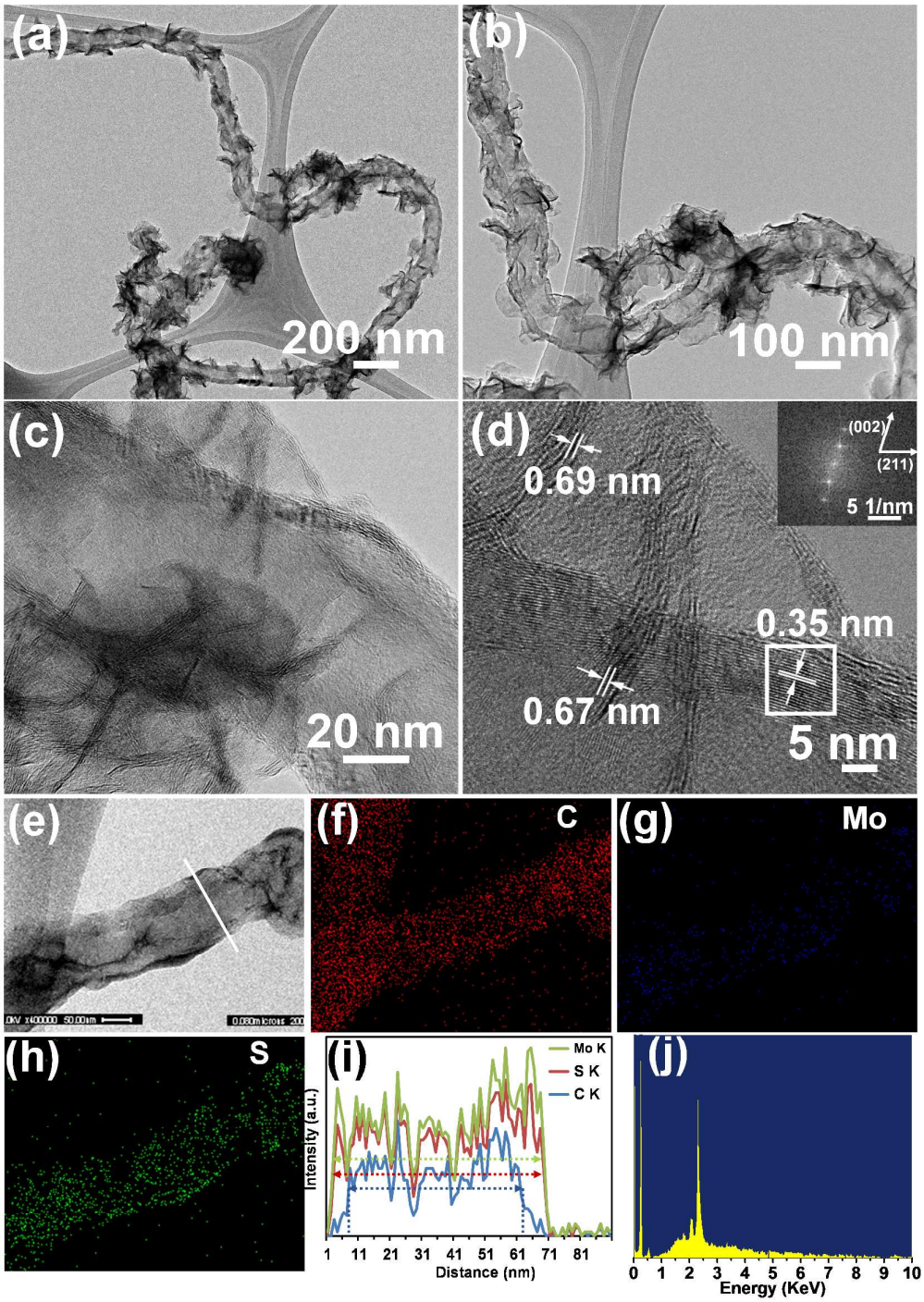

Figure 3 TEM image (a) and (b), and HRTEM image (c) and (d) of MoS_2 architectures@GF/CNT foam. Inset in Figure 3 (d) shows the FFT pattern taken from the marked area. (e-h) EDS mapping of MoS_2 nanosheets@GF/CNT. (i) and (j) HR-EDS line profile and corresponding EDS spectrum of MoS_2@GF/CNT.

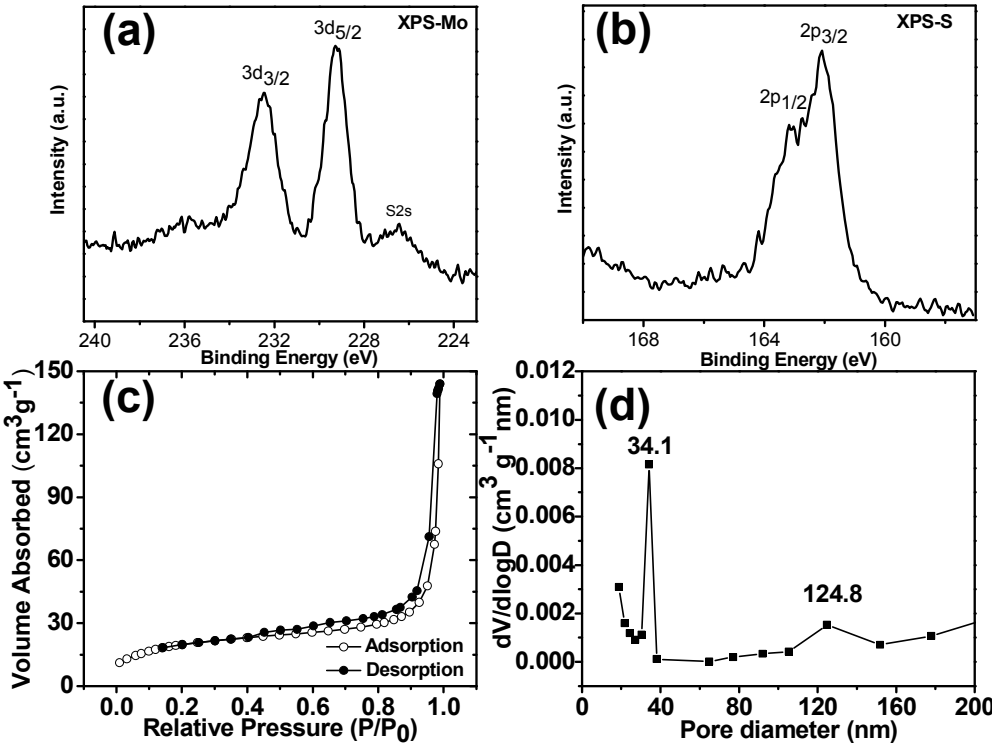

Figure 4 XPS spectra of a) Mo 3d and S 2s peaks, and b) S 2p peaks. c) N_2 adsorption/desorption isotherms, and d) corresponding pore size distribution of MoS_2@GF/CNT.

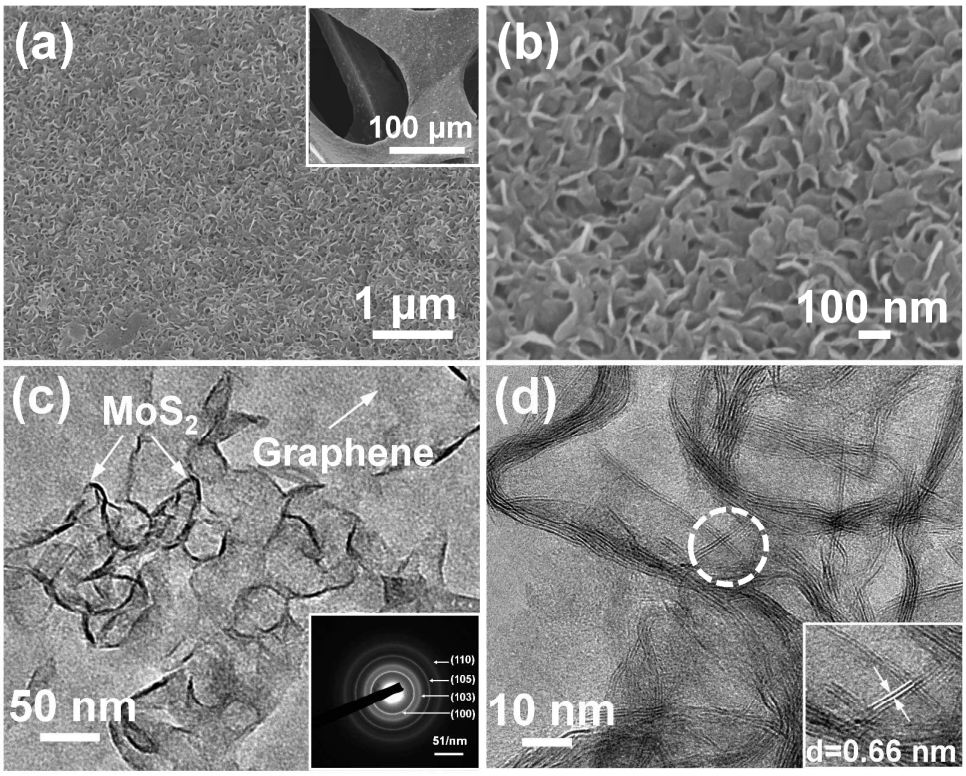

Figure 5. SEM image (a and b) (fine structures in inset of Figure 5a). (c) TEM image and (d) HRTEM images of MoS_2@GF. The insets of Figure 5c shows SAED pattern. The inserted HRTEM image with d-space of 0.66 nm is enlarged regions of the dashed circles.

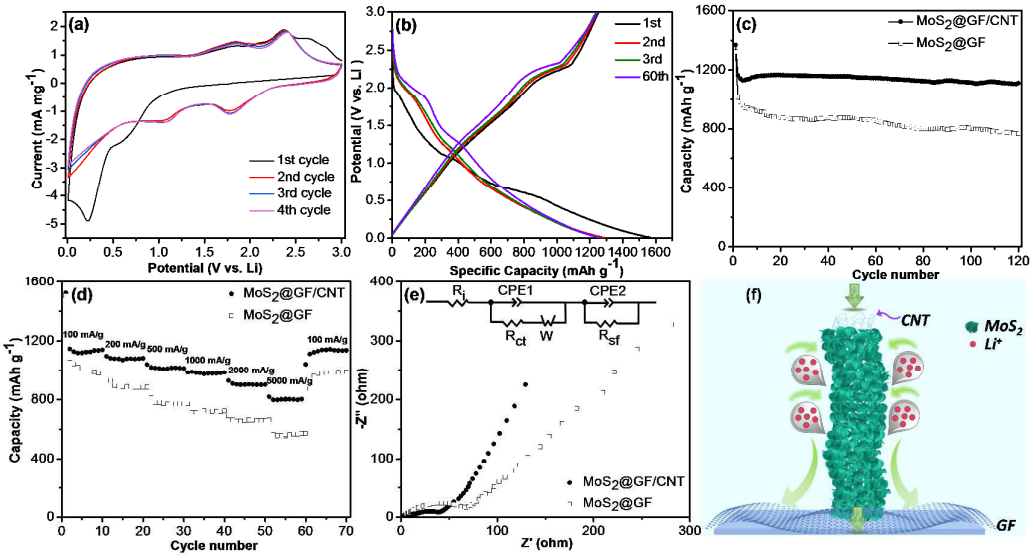

Figure 6. Electrochemical characterization of the MoS_2@GF/CNT electrode as the anode of lithium ion batteries: (a) The first 4 cycles CV curves at a scan rate of 0.2 mV s^{-1}, b) the charge and discharge curves at a current density of 100 mAh g^{-1}, c) cycling behaviors at a current density of 200 mAh g^{-1}, d) cycling behavior at various current densities, e) Nyquist plots over the frequency range from 200 KHz to 0.01 Hz. (the equivalent circuit model of the studied system, inset), f) Schematic illustration of convenient electrolyte ions diffusion and fast transportation of electron in MoS_2 architectures@GF/CNT electrode.

Graphical Abstract

The sp^2-hybridized GF/CNT film provides a robust framework with an ideal contact for boosting vast growth of MoS_2 nanosheets and immobilizing them, in favor for an increased areal loading but improved stability of active materials.